

Unveiling the key factor for the phase reconstruction and exsolved metallic particle distribution in perovskites

Hyunmin Kim

Ulsan National Institute of Science and Technology

Chasung Lim

Pohang University of Science and Technology

Ohhun Kwon

Ulsan National Institute of Science and Technology

Hu Young Jeong

Ulsan National Institute of Science and Technology <https://orcid.org/0000-0002-5550-5298>

Sihyuk Choi

Kumoh National Institute of Technology

Jeong Woo Han

Pohang University of Science and Technology <https://orcid.org/0000-0001-5676-5844>

Guntae Kim (✉ gtkim@unist.ac.kr)

Ulsan National Institute of Science and Technology <https://orcid.org/0000-0002-5167-0982>

Article

Keywords: Exsolution of Transition Metals, Intelligent Catalyst Design, Ruddlesden-Popper Perovskite, Phase Reconstruction, Oxygen Vacancy Formation Energies

Posted Date: March 29th, 2021

DOI: <https://doi.org/10.21203/rs.3.rs-313845/v1>

License: © ⓘ This work is licensed under a Creative Commons Attribution 4.0 International License.

[Read Full License](#)

Version of Record: A version of this preprint was published at Nature Communications on November 24th, 2021. See the published version at <https://doi.org/10.1038/s41467-021-26739-1>.

Unveiling the key factor for the phase reconstruction and exsolved metallic particle distribution in perovskites

Hyunmin Kim^{a,†}, Chaesung Lim^{b,†}, Ohhun Kwon^{c,†}, Hu Young Jeong^d, Sihyuk Choi^{e,*}, Jeong Woo Han^{b,*} and Guntae Kim^{a,*}

Affiliation

^a School of Energy and Chemical Engineering, Ulsan National Institute of Science and Technology (UNIST), Ulsan, 44919, Republic of Korea

^b Department of Chemical Engineering, Pohang University of Science and Technology (POSTECH), Pohang 37673, Republic of Korea

^c Department of Chemical and Biomolecular Engineering, University of Pennsylvania, Philadelphia, Pennsylvania 19104, United States of America.

^d Department of Materials Science and Engineering and UNIST Central Research Facilities (UCRF), Ulsan National Institute of Science and Technology (UNIST), Ulsan, 44919, Republic of Korea

^e Department of Aeronautics, Mechanical and Electronic Convergence Engineering, Kumoh National Institute of Technology, Gyeongbuk 39177, Republic of Korea.

[†] These authors contributed equally to this work.

* Corresponding authors.

Email: sh.choi@kumoh.ac.kr (S.C.), jwhan@postech.ac.kr (J.W.H.), gtkim@unist.ac.kr (G.K.).

Abstract

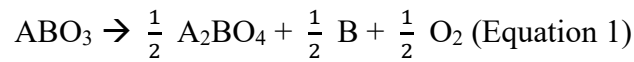
The exsolution of transition metals in perovskite oxides has been actively researched for intelligent catalyst design in energy-related applications. To significantly increase the amount of exsolved particles, the complete phase reconstruction from simple perovskite to Ruddlesden-Popper (R-P) perovskite is greatly desirable. However, a comprehensive understanding of key parameters affecting the phase reconstruction to R-P perovskite is still unexplored. Herein, the oxygen vacancy formation energies (E_{v-f-O}) from PrO and TO_2 in $\text{Pr}_{0.5}(\text{Ba/Sr})_{0.5}\text{TO}_{3-\delta}$ ($T = \text{Mn, Fe, Co, and Ni}$) are proposed as the important factor in determining the type of phase reconstruction in perovskites. Furthermore, using *in-situ* temperature & environment-controlled X-ray diffraction measurements, we mapped out the phase diagram and found the optimum 'x' range required for the complete phase reconstruction to R-P perovskite ($x \geq 0.3$) in $\text{Pr}_{0.5}\text{Ba}_{0.5-x}\text{Sr}_x\text{FeO}_{3-\delta}$ (PBSF) system. Among PBSF, the $(\text{Pr}_{0.5}\text{Ba}_{0.2}\text{Sr}_{0.3})_2\text{FeO}_{4+\delta} - \text{Fe}$ metal (R-PBSF30) has the smallest size of exsolved Fe metal particles when the phase reconstruction occurs from simple perovskite under reducing condition. The exsolved nano-Fe metal particles exhibited high particle density and are well-distributed on the perovskite surface, showing great catalytic activity in fuel cell mode (1.23 W cm^{-2} at 800°C) and high syngas production by co-electrolysis of CO_2 and H_2O (-1.62 A cm^{-2} at 1.5 V , 800°C).

Introduction

Tailoring the functionality of perovskite oxides (ABO_3) by decorating the surface with catalytically active particles plays an important role in energy-related applications such as fuel cells, electrolysis cells, metal-air batteries, and supercapacitors¹⁻⁶. The catalyst particles are typically prepared by deposition techniques (*e.g.* infiltration, chemical vapor deposition, and pulsed laser deposition), in which the catalysts are embedded onto the surface from external precursors⁷⁻⁹. However, these techniques require redundant heat-treatments for preparation and the catalyst particles suffer from agglomeration and/or coarsening over time, resulting in performance degradation^{10,11}. In this respect, it is of great importance to develop more robust and time-efficient catalyst preparation method. Exsolution phenomenon on the basis of *in-situ* growth of metal particles has been suggested as an advanced approach to designing perovskite matrix with electro-catalytically active particles^{12,13}. In this approach, catalytically-active metal elements (*e.g.* Pd, Ru, Co, Ni, and Fe, *etc...*) are initially incorporated into the B-site of perovskite oxides, and then exsolved as metallic particles from the perovskite support under reducing atmosphere^{14,15}. As compared with the conventional catalyst preparation methods, the *in-situ* exsolution process provides benefits of time-efficient catalyst preparation, enhanced catalyst lifetime, and robust thermal stability^{16,17}. Notwithstanding the advantages, two major thresholds hinder the practical application of the exsolution process: (i) restricted diffusion of catalytically active cations to the surface due to preferential segregation within the bulk¹⁸, and (ii) structural destruction and/or insulating phase evolution after excessive cation defect formation¹⁹.

In order to address the challenges of the exsolution phenomenon, A-site deficient perovskites ($A/B < 1$) has been extensively employed as an attractive methodology^{2,20-22}. In A-site deficient perovskites, formation of oxygen vacancies is promoted by phase stabilization

from non-stoichiometric perovskite to “defect-free” perovskite under reducing condition, facilitating the B-site exsolution^{23,24}. Hence, the B-site exsolution level is proportional to A-site deficiency range (‘ α ’ for $A_{1-\alpha}BO_{3-\delta}$). Meanwhile, there exists restriction in the variation of A-site deficiency range (about $0 < \alpha < 0.2$ for $A_{1-\alpha}BO_{3-\delta}$) because excessive A-site deficiency may be accompanied by formation of undesirable A-site oxide phases^{19,25}. Given these aspects, an alternative corresponding method to further trigger the B-site exsolution is using the *in-situ* phase reconstruction from simple perovskite to Ruddlesden-Popper (R-P) perovskite oxides ($A_{n+1}B_nO_{3n+1}$ with $n = 1, 2,$ and 3) *via* reduction process^{26,27}. This strategy facilitates abundant formation of oxygen vacancies during the phase reconstruction, breaking the bottleneck of exsolution capability.



From equation 1, it is presumable that considerable number of cations at B-site will be reduced into metals without A-site segregation after phase reconstruction from simple perovskite (ABO_3) to $n = 1$ R-P perovskite (A_2BO_4). Although several perovskites have exhibited superior distribution of catalyst particles on the surface *via* phase transition to R-P perovskite²⁸⁻³⁰, the comprehensive understanding of key factors modulating the phase reconstruction to R-P perovskite is still an open question.

Inspired by the above perspectives, the goal of this study is to identify the significant factor contributing to the phase reconstruction from simple perovskite to R-P perovskite. Here, we systematically calculated the oxygen vacancy formation energies (E_{vf-O}) of perovskite oxides with various cations to investigate the unprecedented factor affecting the phase reconstruction. The type of phase reconstruction could be predicted with the E_{vf-O} value from PrO and TO_2 networks in $Pr_{0.5}(Ba/Sr)_{0.5}TO_{3-\delta}$ ($T = Mn, Fe, Co,$ and Ni), in which the most appropriate cations for the complete reconstruction to R-P perovskite were determined. Afterwards, the phase

diagram obtained from *in-situ* temperature & environment-controlled X-ray diffraction measurements revealed the phase reconstruction tendency of $\text{Pr}_{0.5}\text{Ba}_{0.5-x}\text{Sr}_x\text{FeO}_{3-\delta}$ ($x = 0, 0.1, 0.2, 0.3, 0.4$ and 0.5 , abbreviated as “PBSF” in **Supplementary Table 1**) materials with respect to ‘ x ’ value and reduction temperature. Furthermore, the as-exsolved Fe metal particle size and distribution for PBSF after reduction process were observed from microscopy analysis. In accordance with the theoretical calculations and experimental data, $\text{Pr}_{0.5}\text{Ba}_{0.2}\text{Sr}_{0.3}\text{FeO}_{3-\delta}$ (A-PBSF30) was adopted as the optimized electrode material for symmetrical solid oxide cell (S-SOC) and demonstrated exceptional electrochemical performance (1.23 W cm^{-2} at 800°C under fuel cell mode and -1.62 A cm^{-2} at 800°C under co-electrolysis mode).

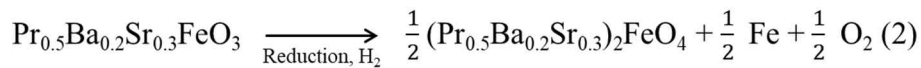
Results

Density functional theory calculations

The complete phase reconstruction from simple perovskite (ABO_3) to Ruddlesden-Popper (R-P) perovskite (A_2BO_4) *via* reduction is considered as one of the efficient strategies to significantly boost the population of exsolved particles. However, the key factors contributing to the phase reconstruction to R-P perovskite has not been investigated. To determine the unexplored factor for the phase reconstruction for the first time, the oxygen vacancy formation energies (E_{vf-O}) from AO (A-site) and BO_2 (B-site) networks were calculated for $Pr_{0.5}Ba_{0.5}TO_{3-\delta}$ and $Pr_{0.5}Sr_{0.5}TO_{3-\delta}$ (T = Mn, Fe, Co, and Ni) perovskite oxides (**Figure 1**)³¹⁻³⁴. For the perovskite oxides to undergo phase reconstruction without phase decomposition under reducing condition, the A-site E_{vf-O} value should be higher than 1.5 eV. Moreover, the B-site E_{vf-O} value would be an important factor for determining the type of phase reconstruction. For instance, the B-site E_{vf-O} should be in the range of about 1.6 to 2.8 eV to demonstrate phase reconstruction to R-P perovskite in the reduction environment. Considering the aforementioned results, only $Pr_{0.5}Sr_{0.5}MnO_{3-\delta}$ (PSM) and $Pr_{0.5}Sr_{0.5}FeO_{3-\delta}$ (PSF) are the possible candidates for the phase reconstruction to R-P perovskite in this study. Among the two potential candidates, we adopted Fe cation as the more suitable B-site cation because of its much superior catalytic activity for fuel oxidation reaction rather than Mn cation¹⁸. Accordingly, we systematically analyzed the phase reconstruction tendency of $Pr_{0.5}Ba_{0.5-x}Sr_xFeO_{3-\delta}$ ($x = 0, 0.1, 0.2, 0.3, 0.4,$ and 0.5 , abbreviated as “PBSF” in **Supplementary Table 1**) materials with respect to different Ba^{2+}/Sr^{2+} ratio.

Structural characterization

Before examining the phase reconstruction tendency of PBSF, the crystalline structures after heat-treated in two different environmental conditions were analyzed by X-ray diffraction (XRD) and Rietveld refinement profiles (**Supplementary Figure 1, Supplementary Figure 2, and Supplementary Table 2**). The air-sintered PBSF are all corresponded to simple perovskite structure without detectable secondary phases. On the other hand, after reduction in H₂ atmosphere, the PBSF samples were surprisingly changed to different types of phase depending on the Sr²⁺ concentration. As shown in **Supplementary Figure 2b**, Pr_{0.5}Ba_{0.5}FeO_{3-δ} (A-PBSF00), Pr_{0.5}Ba_{0.2}Sr_{0.3}FeO_{3-δ} (A-PBSF30), and Pr_{0.5}Sr_{0.5}FeO_{3-δ} (A-PBSF50) were changed to Pr_{0.5}Ba_{0.5}FeO_{3-δ} – Fe metal & Pr oxide (R-PBSF00), (Pr_{0.5}Ba_{0.2}Sr_{0.3})₂FeO_{4+δ} – Fe metal (R-PBSF30), and (Pr_{0.5}Sr_{0.5})₂FeO_{4+δ} – Fe metal (R-PBSF50), respectively. Only catalytically active Fe metal peaks along with complete phase reconstruction to R-P perovskite are observed for R-PBSF30 and R-PBSF50, while R-PBSF00 shows Fe metal and Pr oxide segregation without phase reconstruction under reducing condition. Based on the further Rietveld refinement analysis in **Supplementary Figure 3**, R-PBSF30 clearly exhibits the complete phase reconstruction to R-P perovskite with tetragonal structure (space group *I4/mmm* with lattice parameters of a = b = 3.881 and c = 12.713 Å). The complete phase reconstruction could be also described by equation (2), of which considerable amounts of Fe metal are expected to be exsolved in the reduction environment.



Phase reconstruction tendency analysis from phase diagram

To precisely analyze the phase reconstruction tendency for Pr_{0.5}Ba_{0.5-x}Sr_xFeO_{3-δ} (x = 0, 0.1, 0.2, 0.25, 0.3, 0.4, and 0.5) materials, *in-situ* XRD measurements were systematically

conducted in various reduction temperatures and Sr^{2+} concentrations. (**Figure 2a** and **Supplementary Figure 4**). **Figure 2b** displays the proposed phase diagram and the corresponding plotted points after *in-situ* XRD measurements in H_2 with elevating temperature intervals of 10 °C. The A-PBSF00 sample remained simple perovskite structure for all reduction temperature range and co-segregation of Fe metal and Pr oxide were observed simultaneously at the reduction temperature higher than 840 °C (Region II in **Figure 2b**). Even though there was noticeable phase reconstruction for all Sr^{2+} -doped samples, complete phase reconstruction to R-P perovskite was not accomplished for $\text{Pr}_{0.5}\text{Ba}_{0.4}\text{Sr}_{0.1}\text{FeO}_{3-\delta}$ (A-PBSF10), $\text{Pr}_{0.5}\text{Ba}_{0.3}\text{Sr}_{0.2}\text{FeO}_{3-\delta}$ (A-PBSF20), and $\text{Pr}_{0.5}\text{Ba}_{0.25}\text{Sr}_{0.25}\text{FeO}_{3-\delta}$ (A-PBSF25) even at the reduction temperature of 870 °C. (Region III in **Figure 2b**). On the contrary, complete phase reconstruction to R-P perovskite is observed for A-PBSF30, $\text{Pr}_{0.5}\text{Ba}_{0.1}\text{Sr}_{0.4}\text{FeO}_{3-\delta}$ (A-PBSF40), and A-PBSF50 at the reduction temperature of approximately 850 °C (Region IV in **Figure 2b**). These results indicate that the ‘x’ value in PBSF should be at least approximately 0.3 along with the reduction temperature of about 850 °C to accomplish complete phase reconstruction, as illustrated in **Figure 2c**.

Effect of Sr^{2+} concentration on computational calculations

The role of Sr^{2+} concentration in PBSF in terms of phase reconstruction tendency to R-P perovskite was additionally explored using density functional theory (DFT) calculations. **Figure 2d** shows the required total energies for the phase reconstruction (E_{recon}) from simple perovskite to R-P perovskite of four model structures with different $\text{Ba}^{2+}/\text{Sr}^{2+}$ ratio. The E_{recon} decreases with increasing Sr^{2+} concentration in PBSF, indicating that the incorporation of Sr^{2+} into Ba^{2+} site promotes the phase reconstruction to R-P perovskite. Furthermore, the $E_{\text{vf-O}}$ of four simple perovskite models are calculated in **Figure 2e**. More negative $E_{\text{vf-O}}$ value mainly

implies easier formation of oxygen vacancies in the reduction environment³⁵. The E_{vf-O} value becomes more negative after doping Sr^{2+} into Ba^{2+} , revealing that the Sr^{2+} doping facilitates the formation of oxygen vacancies in the reduction atmosphere. This trend could be elucidated by the decrease in tolerance factor after replacement of Ba^{2+} by Sr^{2+} (**Supplementary Table 3**)³⁶. A co-segregation energy (E_{co-seg}) associated to the degree of exsolution for B-site transition metal cations under reducing condition is also calculated (**Figure 2e**). Interestingly, E_{co-seg} decreased as the Sr^{2+} contents increased, suggesting the enhanced degree of Fe exsolution with increasing Sr^{2+} concentration.

Transmission electron microscopy analysis

On the basis of proposed phase diagram and DFT calculations, the A-PBSF30, the minimum Sr^{2+} -doped sample demonstrating complete reconstruction to R-P perovskite, is selected as the target material for structural analysis. The transmission electron microscopy (TEM) and scanning TEM (STEM) analysis were successfully performed to visually probe the complete phase reconstruction from simple perovskite to R-P perovskite of A-PBSF30 material (**Figure 3** and **Supplementary Figure 5**). From the high-resolution TEM images and corresponding fast-Fourier transformed (FFT) patterns, the lattice spaces between planes of A-PBSF30 and R-PBSF30 are 0.395 nm (**Figure 3a**) and 0.634 nm (**Figure 3c**), which are consistent with the lattice constant of (001) plane for simple perovskite and the lattice constant of (002) plane for R-P perovskite, respectively. Furthermore, the atomic-scale observations of A-PBSF30 and R-PBSF30 were definitely validated from high-angle annular dark-field (HAADF) STEM images, of which only technically elusive [100] direction is mandatory for R-P perovskite. The locations of cations are well-matched with the simple perovskite (**Figure 3b**) and R-P perovskite (**Figure 3d**) because the atomic column intensity is proportional to the

Z^{-2} (Z is the atomic number)³⁷, thereby the bright and dark columns are the A-site (*i.e.*, Pr, Ba, and Sr) and the B-site (*i.e.*, Fe), respectively, in the HAADF-STEM mode.

Examination and characterization of exsolved particle size

In general, particle size and surface distribution of catalysts have a considerable influence on the catalytic activity^{4,38}. As such, the particle size and surface distribution of exsolved metal particles *via* reduction treatment could impact on the electro-catalytic activity of catalysts. Before examining the electro-catalytic effect of the *in-situ* exsolved Fe metal particles, an explicit comparison of exsolved particle size and surface distribution for R-PBSF00, R-PBSF30, and R-PBSF50 samples were presented in scanning electron microscope (SEM) images (**Figure 3e**, **Figure 3f**, **Supplementary Figure 6**, and **Supplementary Figure 7**). As shown in **Figure 3f**, many small particles with size of about 100 to 200 nm are observed and uniformly socketed onto the perovskite oxide matrix after reduction, which are speculated as Fe metal particles. In contrast, the size of exsolved particles was relatively larger for R-PBSF00 and R-PBSF50 (**Supplementary Figure 6**, **Supplementary Figure 7**, **Supplementary Figure 8**, and **Supplementary Figure 9**). The energy dispersive spectroscopy (EDS) spectrum and the elemental mapping images of R-PBSF30 also clearly revealed that Fe metal particle with size of about 150 nm is well-socketed onto the R-P perovskite after reduction (**Figure 3g** and **Figure 3h**). Furthermore, the presence of $\text{Fe}^0 2p_{1/2}$ peak for only R-PBSF30 from X-ray photoelectron spectroscopy (XPS) measurements confirm the exsolution of Fe metal onto the surface under reducing condition³⁹, in coincidence with the above experimental results (**Supplementary Figure 10**). To investigate the electrically conductive properties of the exsolved Fe metal particles, the electrical conductivities as a function of temperature under reducing atmosphere were measured for PBSF (**Supplementary Figure 11**). The A-PBSF30 displayed the highest

electrical conductivity value compared to other PBSF in the reduction environment coupled with sufficiently high electrical conductivity in the air atmosphere (**Supplementary Figure 11b**), suggesting that the A-PBSF30 is the potential electrode material for symmetrical solid oxide cell (S-SOC) electrode material.

Electrochemical performance evaluation

Prior to assessment of electrochemical performance for A-PBSF30 in the practical application of S-SOCs, great thermo-chemical compatibility between all PBSF and the $\text{La}_{0.9}\text{Sr}_{0.1}\text{Ga}_{0.8}\text{Mg}_{0.2}\text{O}_{3-\delta}$ (LSGM) electrolyte were confirmed by XRD measurement (**Supplementary Figure 12**). Moreover, similar microstructures of air-sintered PBSF samples implies that the electrochemical performance would not be affected by surface morphology (**Supplementary Figure 13**). Then, electrochemical performance of symmetrical solid oxide fuel cells (S-SOFCs) using PBSF as both electrodes were characterized by LSGM electrolyte-supported cells to identify the huge impact of the exsolved Fe metal particle size and surface distribution (**Figure 4a** and **Supplementary Figure 14**). The peak power density of the A-PBSF30 symmetrical cell is 1.23 W cm^{-2} at $800 \text{ }^\circ\text{C}$ with humidified H_2 (3% H_2O) as fuel. This outstanding cell performance is the highest out of open literature based on LSGM electrolyte-supported S-SOFCs without any external catalysts at $800 \text{ }^\circ\text{C}$ under humidified H_2 (3% H_2O) as fuel to our best knowledge (**Figure 4b** and **Table 1**)^{28,39-45}. In addition, peak power outputs of 0.73 W cm^{-2} in humidified C_3H_8 (3% H_2O) at $800 \text{ }^\circ\text{C}$ (**Figure 4c** and **Supplementary Figure 15**). Furthermore, the A-PBSF30 symmetrical cell demonstrated fairly stable current density without observable degradation for about 200 hours in H_2 and 150 hours in C_3H_8 (**Figure 4d** and **Figure 4e**). We also evaluated the electrochemical performance of the A-PBSF30 symmetrical cell in co-electrolysis mode. The excellent current density of -1.62 A cm^{-2} at a

cell voltage of 1.5 V (close to thermo-neutral voltage)⁴⁶ at 800 °C under co-electrolysis condition was demonstrated for the A-PBSF30 symmetrical cell (**Figure 4f**), which is exceptionally high compared to other oxygen-conducting solid oxide electrolysis cell (SOEC) systems with different electrode materials^{19,31,47,48}. Together with superior electrochemical performance, relatively constant voltage was observed for 100 hours under a constant current load of -0.25 A cm^{-2} at 700 °C in co-electrolysis mode (**Figure 4g**), representing great durability in continuous SOEC operation. It is noteworthy that *in-situ* exsolution of well-dispersed Fe metal particles after complete phase reconstruction to R-P perovskite matrix acts as catalysts with promising electro-catalytic activity, leading to outstanding electrochemical performances in various applications.

Discussion

In summary, this study successfully calculated $E_{\text{Vf-O}}$ value from PrO and TO_2 in $\text{Pr}_{0.5}(\text{Ba/Sr})_{0.5}\text{TO}_{3-\delta}$ ($T = \text{Mn, Fe, Co, and Ni}$) as the key factor for identifying the type of the phase reconstruction. Remarkably, the phase diagram acquired from *in-situ* temperature & environment-controlled XRD measurements indicated that the complete phase reconstruction to R-P perovskite occurs at least approximately $x = 0.3$ above at the reduction temperature of 850 °C for PBSF system. Among PBSF with complete phase reconstruction, the highly-populated Fe metal particles socketed on R-PBSF30 attributed to excellent electrochemical performances under both fuel cell (1.23 W cm⁻² at 800 °C under H₂ fuel) and electrolysis cell (−1.62 A cm⁻² at 1.5 V and 800 °C under CO₂ & H₂O fuels) modes coupled with great durability. Our investigations strongly provide a pathway to explore new factors for the phase reconstruction and offer a new opportunity to discover prospective candidates with customized functionalities for next-generation energy-related applications.

Methods

Material synthesis

$\text{Pr}_{0.5}\text{Ba}_{0.5-x}\text{Sr}_x\text{FeO}_{3-\delta}$ samples ($x = 0, 0.1, 0.2, 0.3, 0.4,$ and 0.5 , abbreviated as PBSF in **Supplementary Table 1**) were synthesized by the Pechini method. Stoichiometric amounts of $\text{Pr}(\text{NO}_3)_3 \cdot 6\text{H}_2\text{O}$ (Aldrich, 99.9%, metal basis), $\text{Ba}(\text{NO}_3)_2$ (Aldrich, 99+%), $\text{Sr}(\text{NO}_3)_2$ (Aldrich, 99+%) and $\text{Fe}(\text{NO}_3)_3 \cdot 9\text{H}_2\text{O}$ (Aldrich, 98+%) nitrate salts were dissolved in distilled water with the addition of quantitative amounts of citric acid and poly-ethylene glycol. After removal of excess resin by heating at $280\text{ }^\circ\text{C}$, transparent organic resins containing metals in a solid solution were formed. The resins were calcined at $600\text{ }^\circ\text{C}$ for 4 hours and then sintered at $1200\text{ }^\circ\text{C}$ for 4 hours in air environment. The chemical compositions of the synthesized powders and their abbreviations are given in **Supplementary Table 1**.

Structural characterization

The crystal structure of the $\text{Pr}_{0.5}\text{Ba}_{0.5-x}\text{Sr}_x\text{FeO}_{3-\delta}$ samples ($x = 0, 0.3,$ and 0.5) after heat-treated in two different environmental conditions (sintered at $1200\text{ }^\circ\text{C}$ for 4 hours in air environment and reduced at $850\text{ }^\circ\text{C}$ for 4 hours in humidified H_2 environment (3% H_2O)) were first identified by powder X-ray diffraction (XRD) patterns (Rigaku diffractometer, $\text{Cu } K\alpha$ radiation, 40 kV, 40 mA) in the 2θ range of $20^\circ < 2\theta < 60^\circ$. To calculate the exact Bravais lattice of the PBSF, the samples were first pressed into pellets at 2 MPa for 30 seconds and then sintered at $1200\text{ }^\circ\text{C}$ for 4 hours in air atmosphere. The XRD patterns of air-sintered PBSF series and $(\text{Pr}_{0.5}\text{Ba}_{0.2}\text{Sr}_{0.3})_2\text{FeO}_{4+\delta}$ –Fe metal (R-PBSF30) samples were further measured by high-power (HP) XRD. (Max 2500V, $\text{Cu } K\alpha$ radiation, 40 kV, 200 mA) at a scanning rate of 1° min^{-1} and a range of $15^\circ < 2\theta < 105^\circ$. After the HP XRD measurement, the powder patterns and lattice

parameters were analyzed by the Rietveld refinement technique using the GSAS II program. The surface analysis of $\text{Pr}_{0.5}\text{Ba}_{0.2}\text{Sr}_{0.3}\text{FeO}_{3-\delta}$ (A-PBSF30) and $(\text{Pr}_{0.5}\text{Ba}_{0.2}\text{Sr}_{0.3})_2\text{FeO}_{4+\delta}$ – Fe metal (R-PBSF30) were conducted on X-ray photoelectron spectroscopy (XPS) analyses on ESCALAB 250 XI from Thermo Fisher Scientific with a monochromated Al- $K\alpha$ (ultraviolet He1, He2) X-ray source.

***In-situ* phase reconstruction tendency evaluation**

The *in-situ* phase reconstruction tendency of $\text{Pr}_{0.5}\text{Ba}_{0.5-x}\text{Sr}_x\text{FeO}_{3-\delta}$ ($x = 0, 0.1, 0.2, 0.25, 0.3, 0.4$ and 0.5) samples were identified by *in-situ* XRD measurements under humidified H_2 condition (3% H_2O). $\text{Pr}_{0.5}\text{Ba}_{0.25}\text{Sr}_{0.25}\text{FeO}_{3-\delta}$ (A-PBSF25) sample was additionally synthesized by the Pechini method to evaluate the trend the phase reconstruction. The $\text{Pr}_{0.5}\text{Ba}_{0.5-x}\text{Sr}_x\text{FeO}_{3-\delta}$ ($x = 0, 0.1, 0.2, 0.25, 0.3, 0.4$ and 0.5) samples were sintered at $1200\text{ }^\circ\text{C}$ for 4 hours in air atmosphere to form simple perovskite structure with fine crystallinity. The reduction temperatures were ranged from $700\text{ }^\circ\text{C}$ to $870\text{ }^\circ\text{C}$ and two hours were delayed at each temperature interval (Bruker D8 advance).

Electron microscopy analysis

The microstructures of $\text{Pr}_{0.5}\text{Ba}_{0.5-x}\text{Sr}_x\text{FeO}_{3-\delta}$ samples ($x = 0, 0.3,$ and 0.5) sintered at $1200\text{ }^\circ\text{C}$ for 4 hours in air atmosphere, reduced at $850\text{ }^\circ\text{C}$ for 4 hours in humidified H_2 environment (3% H_2O), and PBSF samples sintered at $950\text{ }^\circ\text{C}$ for 4 hours in air atmosphere were investigated by using a scanning electron microscope (Nova Nano FE-SEM). Transmission electron microscopy (TEM) analyses were conducted with a JEOL JEM 2100F with a probe forming (STEM) Cs (spherical aberration) corrector at 200 kV .

Electrical conductivity measurements

The electrical conductivities of PBSF with respect to temperature were measured under air and 5% H₂ environments by the 4-probe method. The samples were pressed into pellets of cylindrical shape and then sintered at 1400 °C for 4 hours in air environment to reach an apparent density of approximately 90%. The electrical conductivities were first measured in air atmosphere from 300 °C to 800 °C with intervals of 50 °C, and then measured in wet 5% H₂ atmosphere (Ar balance, 3% H₂O) from 300 °C to 800 °C with intervals of 50 °C. The current and voltage were recorded by a Biologic Potentiostat to calculate the resistance, resistivity, and conductivity of samples.

Computational methods

Density functional theory (DFT) calculations were performed to investigate the appropriate dopants for the phase reconstruction to $n = 1$ R-P perovskite along with the role of Sr²⁺ concentration on phase reconstruction tendency of PBSF using the Vienna ab initio Simulation Package (VASP)^{49,50}. For the exchange-correlation, the generalized gradient approximation (GGA) based Perdew-Burke-Ernzerhof (PBE) functional was used⁵¹. The electron-ion interactions were described using the projector augmented wave (PAW) potential^{52,53}. A plane wave was expanded up to cutoff energy of 400 eV. Electronic occupancies were calculated using Gaussian smearing with a smearing parameter of 0.05 eV. For the bulk optimization, all internal atoms were relaxed using a conjugate gradient algorithm until the forces of each atom were lowered below 0.03 eV/Å with an energy convergence of 10⁻⁵ eV. GGA+ U approach was used to correct the self-interaction errors with $U_{\text{eff}} = 4.0$ eV for Fe 3d orbital, $U_{\text{eff}} = 3.3$ eV for Co 3d orbital, $U_{\text{eff}} = 4.0$ eV for Mn 3d orbital, $U_{\text{eff}} = 7.0$ eV for Ni 3d orbital, and $U_{\text{eff}} = 6.0$ eV for Pr 4f orbital^{18,54,55}. For the Brillouin zones of the formation energy calculation of cubic

perovskite ($2 \times 2 \times 4$ super cell) and $n = 1$ R-P perovskite ($2 \times 2 \times 1$ super cell), $3 \times 3 \times 1$ and $3 \times 3 \times 2$ Monkhorst–Pack k–point sampling were used, respectively⁵⁶. For the oxygen vacancy formation energy calculations of BO₂ layer between two AO layers, PrO-terminated (001) slab model (2×2 surface, 8 layers with 2 fixed bottom layers, vacuum layer of 16 Å) were used. For the co-segregation energy calculations, FeO₂-terminated (001) slab model ($2\sqrt{2} \times 2\sqrt{2}$ surface, 8 layers with 3 fixed bottom layers, vacuum layer of 16 Å) were used. For the Brillouin zones of the oxygen vacancy formation energy and the co-segregation energy calculations, $3 \times 3 \times 1$ and $1 \times 1 \times 1$ Monkhorst-Pack k-point sampling were used. The optimized lattice parameters of four materials, A-PBSF00 (Ba:Sr = 16:0), Pr_{0.5}Ba_{0.1875}Sr_{0.3125}FeO_{3- δ} (Ba:Sr = 6:10), Pr_{0.5}Ba_{0.125}Sr_{0.375}FeO_{3- δ} (Ba:Sr = 4:12), and A-PBSF50 (Ba:Sr = 0:16) were used for model structures in the computational studies. For the Ba²⁺/Sr²⁺ mixed models, the most stable configurations among the total 5 different Ba configurations were used.

The relative energies required for the phase reconstruction from simple perovskite to $n = 1$ R-P perovskite (E_{recon}) of four model structures with different Sr²⁺ concentration were calculated using the total energy difference between simple perovskite and $n = 1$ R-P perovskite by following equation:

$$E_{recon} = \frac{1}{16} E_{R-P \text{ perov}} + \frac{1}{2} E_{Fe} + \frac{1}{2} E_{O_2} - \frac{1}{16} E_{simple \text{ perov}},$$

Where $E_{R-P \text{ perov}}$ and $E_{simple \text{ perov}}$ are the total energy of simple perovskite ($2 \times 2 \times 4$ super cell) and R-P perovskite ($2 \times 2 \times 1$ super cell), E_{Fe} is total energy of body-centered cubic (BCC) Fe metal unit cell, and E_{O_2} is the total energy of gas phase oxygen molecule.

The oxygen vacancy formation energies (E_{v-f-O}) of Pr_{0.5}Ba_{0.5}TO_{3- δ} , Pr_{0.5}Sr_{0.5}TO_{3- δ} (T = Mn, Co, Fe, and Ni), and four model structures with different Sr²⁺ concentrations were calculated using the lattice oxygen on the BO₂ layer since the phase reconstruction from simple perovskite

(ABO_3) to $n = 1$ R-P perovskite (A_2BO_4) requires the formation of both oxygen and B-site vacancies. For the $Pr_{0.5}Ba_{0.5}TO_{3-\delta}$ and $Pr_{0.5}Sr_{0.5}TO_{3-\delta}$ ($T = Mn, Co, Fe, \text{ and } Ni$) models, the most stable structure configurations were utilized for the oxygen vacancy formation energy calculations. For the four computational models with different Sr^{2+} concentrations, the most stable vacancy sites were utilized for Ba^{2+}/Sr^{2+} mixed models with $Ba:Sr = 6:10$ and $Ba:Sr = 4:12$. The E_{vf-O} was calculated by following equation:

$$E_{vf-O} = E_{perov-defect} + \frac{1}{2}E_{O_2} - E_{perov}$$

where $E_{perov-defect}$ and E_{perov} are the total energies of PrO-terminated (001) perovskite slab model with and without the oxygen vacancy, respectively.

The co-segregation energy (E_{co-seg}) is defined as the total energy difference of two surface models that have different vacancy site. The co-segregation energies of four computational models with different Sr^{2+} concentrations were calculated by following equation:

$$E_{co-seg} = E_{(Fe-V_O)_{surface}} - E_{(Fe-V_O)_{bulk}}$$

where $E_{(Fe-V_O)_{surface}}$ and $E_{(Fe-V_O)_{bulk}}$ are total energies of FeO_2 -terminated (001) perovskite slab model that have oxygen vacancy on surface FeO_2 and bulk FeO_2 layer, respectively.

Electrochemical performance measurements

$La_{0.9}Sr_{0.1}Ga_{0.8}Mg_{0.2}O_{3-\delta}$ (LSGM) powder was prepared by conventional solid-state reaction to fabricate LSGM electrolyte-supported symmetrical solid oxide cells (S-SOCs). Stoichiometric amounts of La_2O_3 (Sigma, 99.99%), $SrCO_3$ (Sigma, 99.99%), Ga_2O_3 (Sigma, 99.99%) and MgO (Sigma, 99.9%) powders were first mixed in a mortar and then ball-milled in ethanol for

24 hours to obtain the desired composition. After drying, the obtained powder was calcined at 1000 °C for 6 hours. After formation of LSGM powder with desired stoichiometry, the electrolyte substrate was prepared by pressing at 2 MPa for 30 seconds into cylindrical shape and then sintered at 1475 °C for 5 hours. The thickness of LSGM electrolyte was polished to about 250 μm. A $\text{La}_{0.6}\text{Ce}_{0.4}\text{O}_{2-\delta}$ (LDC) as a buffer layer was also prepared by ball-milling stoichiometric amounts of La_2O_3 (Sigma, 99.99%) and CeO_2 (Sigma, 99.99%) in ethanol for 24 hours and then calcined at 1000 °C for 6 hours. Electrode slurries were prepared by mixing pre-calcined powders of PBSF with an organic binder (Heraeus V006) and acetone in 3:6:0.6 weight ratio. The electrode inks were applied onto the LSGM pellet by a screen-printing method and then sintered at 950 °C for 4 hours in air to achieve the desired porosity. The porous electrodes had an active area of 0.36 cm² and a thickness of about 15 μm. The LDC layer was screen-printed between the electrode and electrolyte to prevent inter-diffusion of ionic species between electrode and electrolyte. The cells with configuration of “Electrode|LDC|LSGM|LDC|Electrode” were mounted on alumina tubes with ceramic adhesives (Ceramabond 552, Aremco) for electrochemical performance tests. Silver paste and silver wire were utilized for electrical connections to both the fuel electrode and air electrode. The entire cell was placed inside a furnace and heated to the desired temperature. I-V polarization curves of synthesized fuel cells with PBSF as both sides of electrodes were measured using a BioLogic Potentiostat in a temperature range of 700 to 800 °C (temperature interval: 50 °C) in humidified hydrogen (3% H₂O) at a flow rate of 100 ml min⁻¹. Fuel cell evaluation under humidified C₃H₈ fuel (3% H₂O) at a flow rate of 100 ml min⁻¹ were also performed for symmetrical solid oxide fuel cell (S-SOFC) test with cell composition A-PBSF30|LDC|LSGM|LDC|A-PBSF30 from 700 °C to 800 °C (temperature interval: 50 °C) using a BioLogic Potentiostat. For the electrochemical performance test of S-SOC with the cell composition of A-PBSF30|LDC|LSGM|LDC|A-PBSF30 during co-electrolysis, 50 ml min⁻¹ of

H₂ and CO₂ into a H₂O-containing bubbler (with a heating tape) were co-fed to fuel electrode and 100 ml min⁻¹ of air was fed to air electrode.

Data Availability

The data measured, simulated, and analyzed in this study are available from the corresponding author on reasonable request.

References

1. Sengodan, S. *et al.* Layered oxygen-deficient double perovskite as an efficient and stable anode for direct hydrocarbon solid oxide fuel cells. *Nat. Mater.* **14**, 205–209 (2015).
2. Neagu, D., Tsekouoras, G., Miller, D. N., Menard, H. & Irvine, J. T. S. *In situ* growth of nanoparticles through control of non-stoichiometry. *Nat. Chem.* **5**, 916–923 (2013).
3. Kang, K. N. *et al.* Co₃O₄ Exsolved Defective Layered Perovskite Oxide for Energy Storage Systems. *ACS Energy Lett.* **5**, 3828–3836 (2020).
4. Joo, S. *et al.* Cation-swapped homogeneous nanoparticles in perovskite oxides for high power density. *Nat. Commun.* **10**, 1–9 (2019).
5. Opitz, A. K. *et al.* Understanding electrochemical switchability of perovskite-type exsolution catalysts. *Nat. Commun.* **11**, 1–10 (2020).
6. Irvine, J. T. S. *et al.* Evolution of the electrochemical interface in high-temperature fuel cells and electrolyzers. *Nat. Energy* **1**, 1–13 (2016).
7. Ding, D., Li, X., Lai, S. Y., Gerdes, K. & Liu, M. Enhancing SOFC cathode performance by surface modification through infiltration. *Energy Environ. Sci.* **7**, 552–575 (2014).
8. Schlupp, M. V. F., Evans, A., Martynczuk, J. & Prestat, M. Micro-solid oxide fuel cell membranes prepared by aerosol-assisted chemical vapor deposition. *Adv. Energy Mater.* **4**, 1–7 (2014).
9. Kwak, N. W. *et al.* *In situ* synthesis of supported metal nanocatalysts through heterogeneous doping. *Nat. Commun.* **9**, 1–8 (2018).

10. Jun, A., Kim, J., Shin, J. & Kim, G. Achieving High Efficiency and Eliminating Degradation in Solid Oxide Electrochemical Cells Using High Oxygen-Capacity Perovskite. *Angew. Chem. Int. Ed.* **55**, 12512–12515 (2016).
11. Choi, S. *et al.* A robust symmetrical electrode with layered perovskite structure for direct hydrocarbon solid oxide fuel cells: $\text{PrBa}_{0.8}\text{Ca}_{0.2}\text{Mn}_2\text{O}_{5+\delta}$. *J. Mater. Chem. A.* **4**, 1747–1753 (2016).
12. Myung, J. H., Neagu, D., Miller, D. N. & Irvine, J. T. S. Switching on electrocatalytic activity in solid oxide cells. *Nature.* **537**, 528–531 (2016).
13. Neagu, D. *et al.* *In Situ* Observation of Nanoparticle Exsolution from Perovskite Oxides: From Atomic Mechanistic Insight to Nanostructure Tailoring. *ACS Nano.* **13**, 12996–13005 (2019).
14. Sun, Y. *et al.* New Opportunity for *in Situ* Exsolution of Metallic Nanoparticles on Perovskite Parent. *Nano Lett.* **16**, 5303–5309 (2016).
15. Kwon, O. *et al.* Self-assembled alloy nanoparticles in a layered double perovskite as a fuel oxidation catalyst for solid oxide fuel cells. *J. Mater. Chem. A.* **6**, 15947–15953 (2018).
16. Joo, S. *et al.* Highly active dry methane reforming catalysts with boosted in situ grown Ni-Fe nanoparticles on perovskite via atomic layer deposition. *Sci. Adv.* **6**, 1–9 (2020).
17. Zhang, J., Gao, M. R. & Luo, J. L. In Situ Exsolved Metal Nanoparticles: A Smart Approach for Optimization of Catalysts. *Chem. Mater.* **32**, 5424–5441 (2020).
18. Kwon, O. *et al.* Exsolution trends and co-segregation aspects of self-grown catalyst nanoparticles in perovskites. *Nat. Commun.* **8**, 1–7 (2017).

19. Liu, S., Liu, Q. & Luo, J. L. Highly Stable and Efficient Catalyst with in Situ Exsolved Fe-Ni Alloy Nanospheres Socketed on an Oxygen Deficient Perovskite for Direct CO₂ Electrolysis. *ACS Catal.* **6**, 6219–6228 (2016).
20. Sun, Y. *et al.* A-site deficient perovskite: The parent for *in situ* exsolution of highly active, regenerable nano-particles as SOFC anodes. *J. Mater. Chem. A.* **3**, 11048–11056 (2015).
21. Tsekouras, G., Neagu, D. & Irvine, J. T. S. Step-change in high temperature steam electrolysis performance of perovskite oxide cathodes with exsolution of B-site dopants. *Energy Environ. Sci.* **6**, 256–266 (2013).
22. Zhu, T., Troiani, H. E., Mogni, L. V., Han, M. & Barnett, S. A. Ni-Substituted Sr(Ti,Fe)O₃ SOFC Anodes: Achieving High Performance via Metal Alloy Nanoparticle Exsolution. *Joule.* **2**, 478–496 (2018).
23. Gao, Y., Chen, D., Saccoccio, M., Lu, Z. & Ciucci, F. From material design to mechanism study: Nanoscale Ni exsolution on a highly active A-site deficient anode material for solid oxide fuel cells. *Nano Energy.* **27**, 499–508 (2016).
24. Kim, K. J. *et al.* Facet-Dependent *in Situ* Growth of Nanoparticles in Epitaxial Thin Films: The Role of Interfacial Energy. *J. Am. Chem. Soc.* **141**, 7509–7517 (2019).
25. Neagu, D. *et al.* Demonstration of chemistry at a point through restructuring and catalytic activation at anchored nanoparticles. *Nat. Commun.* **8**, 1–8 (2017).
26. Yang, C. *et al.* *In situ* fabrication of CoFe alloy nanoparticles structured (Pr_{0.4}Sr_{0.6})₃(Fe_{0.85}Nb_{0.15})₂O₇ ceramic anode for direct hydrocarbon solid oxide fuel cells. *Nano Energy.* **11**, 704–710 (2015).

27. Lv, H. *et al.* In Situ Investigation of Reversible Exsolution/Dissolution of CoFe Alloy Nanoparticles in a Co-doped $\text{Sr}_2\text{Fe}_{1.5}\text{Mo}_{0.5}\text{O}_{6-\delta}$ Cathode for CO_2 Electrolysis. *Adv. Mater.* **32**, 1906193 (2020).
28. Yang, C. *et al.* Sulfur-Tolerant Redox-Reversible Anode Material for Direct Hydrocarbon Solid Oxide Fuel Cells. *Adv. Mater.* **24**, 1439–1443 (2012).
29. Du, Z. *et al.* High-Performance Anode Material $\text{Sr}_2\text{FeMo}_{0.65}\text{Ni}_{0.35}\text{O}_{6-\delta}$ with *In Situ* Exsolved Nanoparticle Catalyst. *ACS Nano.* **10**, 8660–8669 (2016).
30. Chung, Y. S. *et al.* *In situ* preparation of a $\text{La}_{1.2}\text{Sr}_{0.8}\text{Mn}_{0.4}\text{Fe}_{0.6}\text{O}_4$ Ruddlesden-Popper phase with exsolved Fe nanoparticles as an anode for SOFCs. *J. Mater. Chem. A.* **5**, 6437–6446 (2017).
31. Park, S. *et al.* In situ exsolved Co nanoparticles on Ruddlesden-Popper material as highly active catalyst for CO_2 electrolysis to CO. *Appl. Catal. B Environ.* **248**, 147–156 (2019).
32. Kim, K. *et al.* Mechanistic insights into the phase transition and metal ex-solution phenomena of $\text{Pr}_{0.5}\text{Ba}_{0.5}\text{Mn}_{0.85}\text{Co}_{0.15}\text{O}_{3-\delta}$ from simple to layered perovskite under reducing conditions and enhanced catalytic activity. *Energy Environ. Sci.* **14**, 16–18 (2021).
33. Vibhu, V. *et al.* Characterization of $\text{PrNiO}_{3-\delta}$ as oxygen electrode for SOFCs. *Solid State Sci.* **81**, 26–31 (2018).
34. Choi, S. *et al.* Highly efficient and robust cathode materials for low-temperature solid oxide fuel cells: $\text{PrBa}_{0.5}\text{Sr}_{0.5}\text{Co}_{2-x}\text{Fe}_x\text{O}_{5+\delta}$. *Sci. Rep.* **3**, 1–6 (2013).
35. Chen, C. & Ciucci, F. Designing Fe-based oxygen catalysts by density functional

- theory calculations. *Chem. Mater.* **28**, 7058–7065 (2016).
36. Brown, J. J., Ke, Z., Geng, W. & Page, A. J. Oxygen Vacancy Defect Migration in Titanate Perovskite Surfaces: Effect of the A-Site Cations. *J. Phys. Chem. C.* **122**, 14590–14597 (2018).
 37. Kwon, O. *et al.* Probing One-Dimensional Oxygen Vacancy Channels Driven by Cation-Anion Double Ordering in Perovskites. *Nano Lett.* **20**, 8353–8359 (2020).
 38. Neagu, D. *et al.* Nano-socketed nickel particles with enhanced coking resistance grown in situ by redox exsolution. *Nat. Commun.* **6**, 1–8 (2015).
 39. Niu, B. *et al.* In-situ growth of nanoparticles-decorated double perovskite electrode materials for symmetrical solid oxide cells. *Appl. Catal. B Environ.* **270**, 118842 (2020).
 40. Liu, B. Q., Dong, X., Xiao, G., Zhao, F. & Chen, F. A Novel Electrode Material for Symmetrical SOFCs. *Adv. Mater.* **22**, 5478–5482 (2010).
 41. Lu, X. *et al.* Mo-doped $\text{Pr}_{0.6}\text{Sr}_{0.4}\text{Fe}_{0.8}\text{Ni}_{0.2}\text{O}_{3-\delta}$ as potential electrodes for intermediate-temperature symmetrical solid oxide fuel cells. *Electrochim. Acta.* **227**, 33–40 (2017).
 42. He, W., Wu, X., Dong, F. & Ni, M. A novel layered perovskite electrode for symmetrical solid oxide fuel cells: $\text{PrBa}(\text{Fe}_{0.8}\text{Sc}_{0.2})_2\text{O}_{5+\delta}$. *J. Power Sources.* **363**, 16–19 (2017).
 43. Zhang, Y., Zhao, H., Du, Z., Świerczek, K. & Li, Y. High-Performance $\text{SmBaMn}_2\text{O}_{5+\delta}$ Electrode for Symmetrical Solid Oxide Fuel Cell. *Chem. Mater.* **31**, 3784–3793 (2019).

44. Cai, H. *et al.* Cobalt-free $\text{La}_{0.5}\text{Sr}_{0.5}\text{Fe}_{0.9}\text{Mo}_{0.1}\text{O}_{3-\delta}$ electrode for symmetrical SOFC running on H_2 and CO fuels. *Electrochim. Acta.* **320**, 134642 (2019).
45. Lu, C. *et al.* Efficient and stable symmetrical electrode $\text{La}_{0.6}\text{Sr}_{0.4}\text{Co}_{0.2}\text{Fe}_{0.7}\text{Mo}_{0.1}\text{O}_{3-\delta}$ for direct hydrocarbon solid oxide fuel cells. *Electrochim. Acta.* **323**, 134857 (2019).
46. Hansen, J. B. Solid oxide electrolysis - a key enabling technology for sustainable energy scenarios. *Faraday Discuss.* **182**, 9–48 (2015).
47. Zhu, J. *et al.* Enhancing CO_2 catalytic activation and direct electroreduction on *in-situ* exsolved Fe/MnO_x nanoparticles from $(\text{Pr},\text{Ba})_2\text{Mn}_{2-y}\text{Fe}_y\text{O}_{5+\delta}$ layered perovskites for SOEC cathodes. *Appl. Catal. B Environ.* **268**, 118389 (2020).
48. Zhou, Y. *et al.* Enhancing CO_2 electrolysis performance with vanadium-doped perovskite cathode in solid oxide electrolysis cell. *Nano Energy.* **50**, 43–51 (2018).
49. Kresse, G. & Hafner, J. Ab initio molecular dynamics for liquid metals. *Phys. Rev. B* **47**, 558–561 (1993).
50. Sholl, D. & Steckel, J. A. Density functional theory: a practical introduction. John Wiley & Sons, Inc., **2011**
51. Perdew, J. P., Burke, K. & Ernzerhof, M. Generalized Gradient Approximation Made Simple. *Phys. Rev. Lett.* **77**, 3865–3868 (1996).
52. Blöchl, P. E. Projector Augmented-Wave Method. *Phys. Rev. B.* **50**, 17953–17979 (1994).
53. Kresse, G. & Joubert, D. From ultrasoft pseudopotentials to the projector augmented-wave Method. *Phys. Rev. B.* **59**, 1758–1775 (1999).

54. Kirklin, S. *et al.* The Open Quantum Materials Database (OQMD): Assessing the Accuracy of DFT Formation Energies. *npj Comput. Mater.* **1**, 1–15 (2015).
55. Bouadjemi, B.; Bentata, S.; Abbad, A.; Benstaali, W.; Bouhafs, B. Half-metallic ferromagnetism in PrMnO₃ perovskite from first principles calculations. *Solid State Commun.* **168**, 6–10 (2013).
56. Monkhorst, H. J. & Pack, J. D. Special points for Brillouin-zone integrations. *Phys. Rev. B.* **13**, 5188 (1976).

Acknowledgements

This work was supported by Basic Science Research program through the National Research Foundation (NRF) funded by the Ministry of Education (NRF-2018R1A2A1A05077532 and NRF-2019R1C1C1005801).

Author Information

These authors contributed equally to this work: Hyunmin Kim, Chaesung Lim, and Dr. Ohhun Kwon.

Author Contributions

H.K. and O.K. carried out most of the experimental works and contributed to manuscript writing. C.L. performed DFT calculations. H.Y.J. conducted TEM measurements and analyzed the TEM images. S.C., J.W.H. and G.K. designed the experiments and analyzed the data. All authors contributed to the discussions and analysis of the results regarding the manuscript.

Corresponding authors

Correspondence to Sihyuk Choi, Jeong Woo Han, or Guntae Kim.

Ethics declarations

The authors declare no competing interests.

Figures

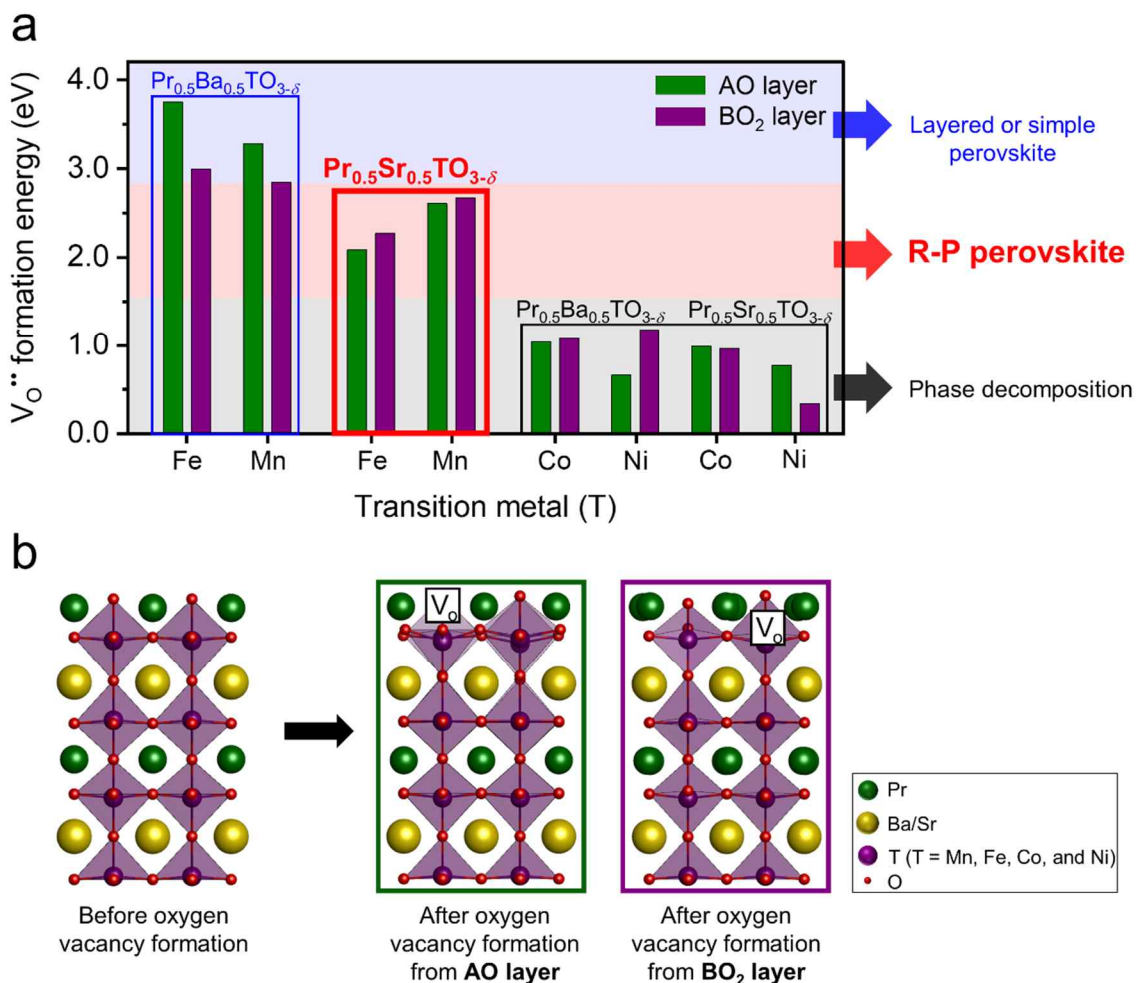


Figure 1. (a) Calculated oxygen vacancy formation energies of $\text{Pr}_{0.5}(\text{Ba}/\text{Sr})_{0.5}\text{TO}_{3-\delta}$ ($T = \text{Mn}, \text{Fe}, \text{Co}, \text{and Ni}$) from AO (green bar) and BO_2 (purple bar) networks and the predicted phase change under reducing condition. (b) Schematic of the most stable structure configurations of $\text{Pr}_{0.5}(\text{Ba}/\text{Sr})_{0.5}\text{TO}_{3-\delta}$ ($T = \text{Mn}, \text{Fe}, \text{Co}, \text{and Ni}$) slab models used for the calculations of oxygen vacancy formation energy values from AO and BO_2 networks.

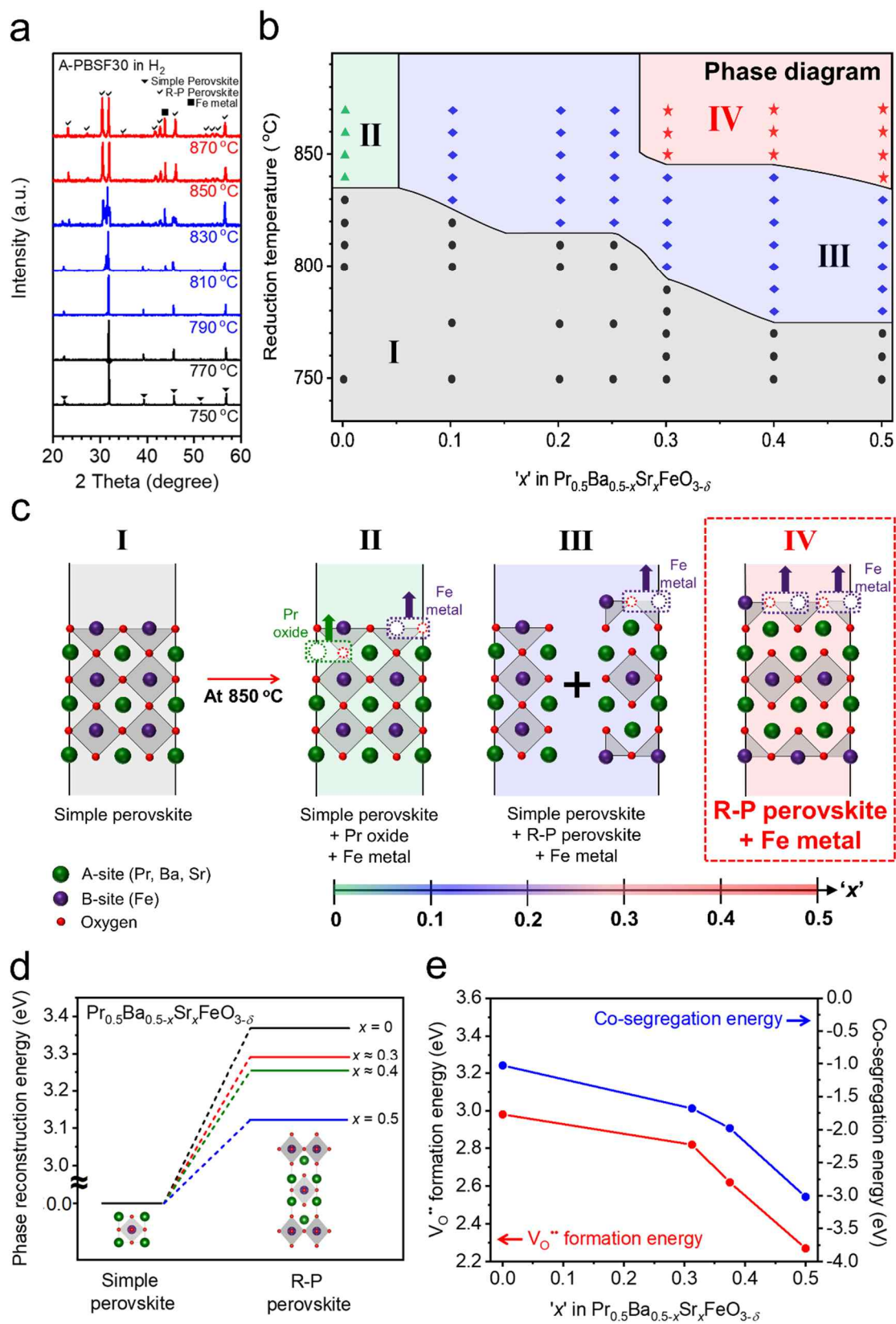


Figure 2. (a – c) Phase reconstruction tendency of $\text{Pr}_{0.5}\text{Ba}_{0.5-x}\text{Sr}_x\text{FeO}_{3-\delta}$ material ($x = 0, 0.1, 0.2, 0.25, 0.3, 0.4$ and 0.5). (a) *In-situ* powder X-ray diffraction (XRD) patterns of

$\text{Pr}_{0.5}\text{Ba}_{0.2}\text{Sr}_{0.3}\text{FeO}_{3-\delta}$ (A-PBSF30) under H_2 environment. (b) Proposed phase diagram of $\text{Pr}_{0.5}\text{Ba}_{0.5-x}\text{Sr}_x\text{FeO}_{3-\delta}$ material ($x = 0, 0.1, 0.2, 0.25, 0.3, 0.4$ and 0.5) in H_2 environment as functions of reduction temperature and Sr^{2+} concentration from *in-situ* X-ray diffraction (XRD) measurements. The phases for region I (gray), II (green), III (blue), and IV (red) are simple perovskite, simple perovskite + Pr oxide + Fe metal, simple perovskite + Ruddlesden-Popper (R-P) perovskite + Fe metal, and R-P perovskite + Fe metal, respectively. (c) Schematic illustration of the above phase diagram. (d – e) Density functional theory (DFT) calculations. Calculated profiles of (d) the relative total energy required for the phase reconstruction from simple perovskite to R-P perovskite and (e) oxygen vacancy formation energies and co-segregation energies as a function of Sr^{2+} concentration in four models.

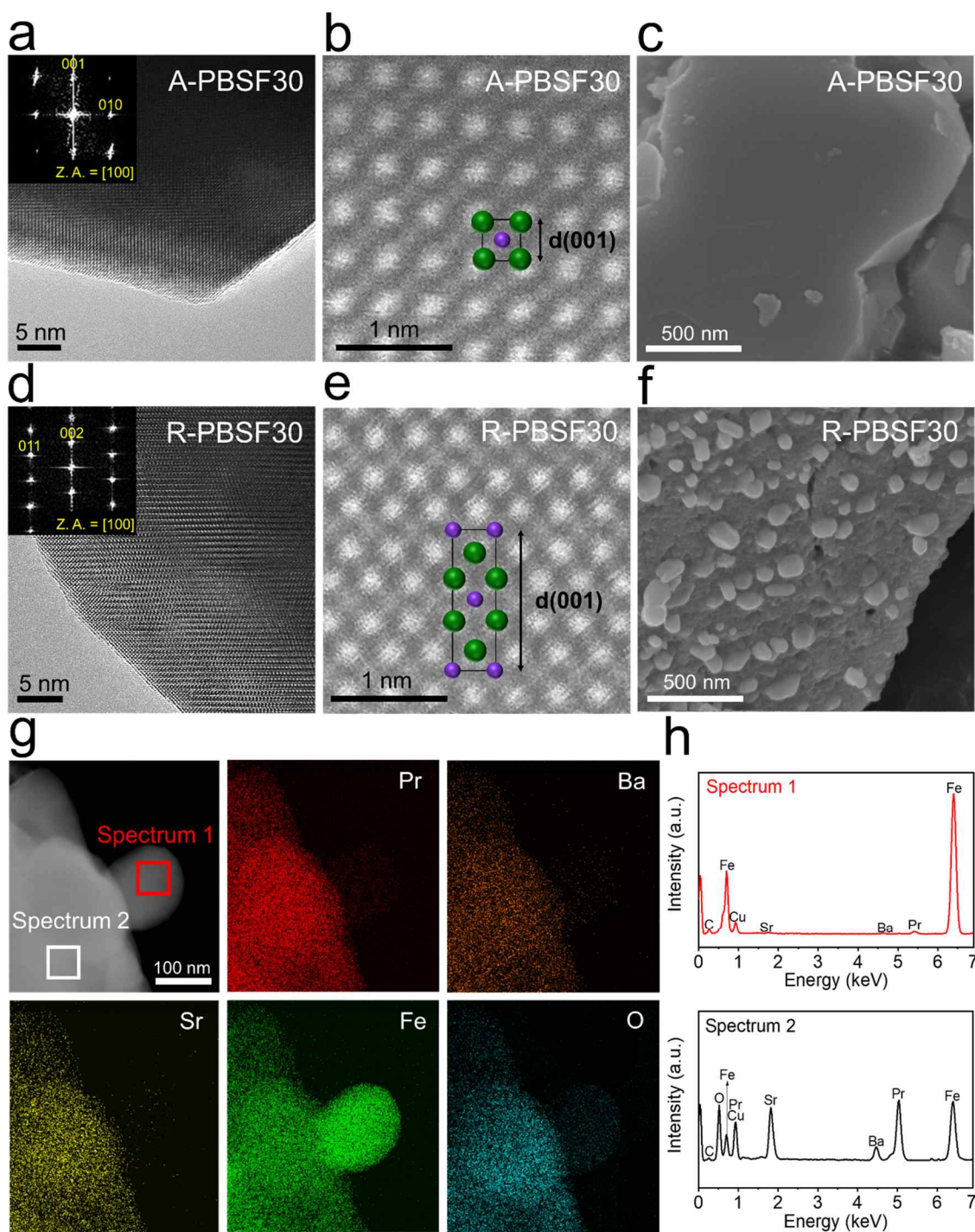


Figure 3. Electron microscopic analysis. (a – b, d – e) Transmission electron microscopy (TEM) analysis. (a) High-resolution (HR) TEM image and the corresponding fast-Fourier transformed (FFT) pattern of $\text{Pr}_{0.5}\text{Ba}_{0.2}\text{Sr}_{0.3}\text{FeO}_{3-\delta}$ (A-PBSF30) with zone axis (Z.A.) = [100] and (b) High-angle annular dark-field (HAADF) scanning TEM (STEM) image of A-PBSF30 with simple perovskite structure of [100] direction with d-spacing 001. (d) HR TEM image and the

corresponding FFT pattern of $(\text{Pr}_{0.5}\text{Ba}_{0.2}\text{Sr}_{0.3})_2\text{FeO}_{4+\delta}$ -Fe metal (R-PBSF30) with Z.A. = [100] and (e) HAADF STEM image and the atomic arrangement of R-PBSF30 of [100] direction with d-spacing 001. (c,f) Scanning electron microscope (SEM) images. SEM images presenting the surface morphologies of (c) A-PBSF30 sintered at 1200 °C for 4 hours in air atmosphere and (f) R-PBSF30 reduced at 850 °C for 4 hours in humidified H_2 environment (3% H_2O). (g – h) TEM-energy dispersive spectroscopy (EDS) analysis. HAADF image of R-PBSF30 and elemental mapping of Pr, Ba, Sr, Fe and O, respectively. (h) EDS spectra of the exsolved Fe metal particle (Spectrum 1) and the parent material $(\text{Pr}_{0.5}\text{Ba}_{0.2}\text{Sr}_{0.3})_2\text{FeO}_{4+\delta}$ (Spectrum 2).

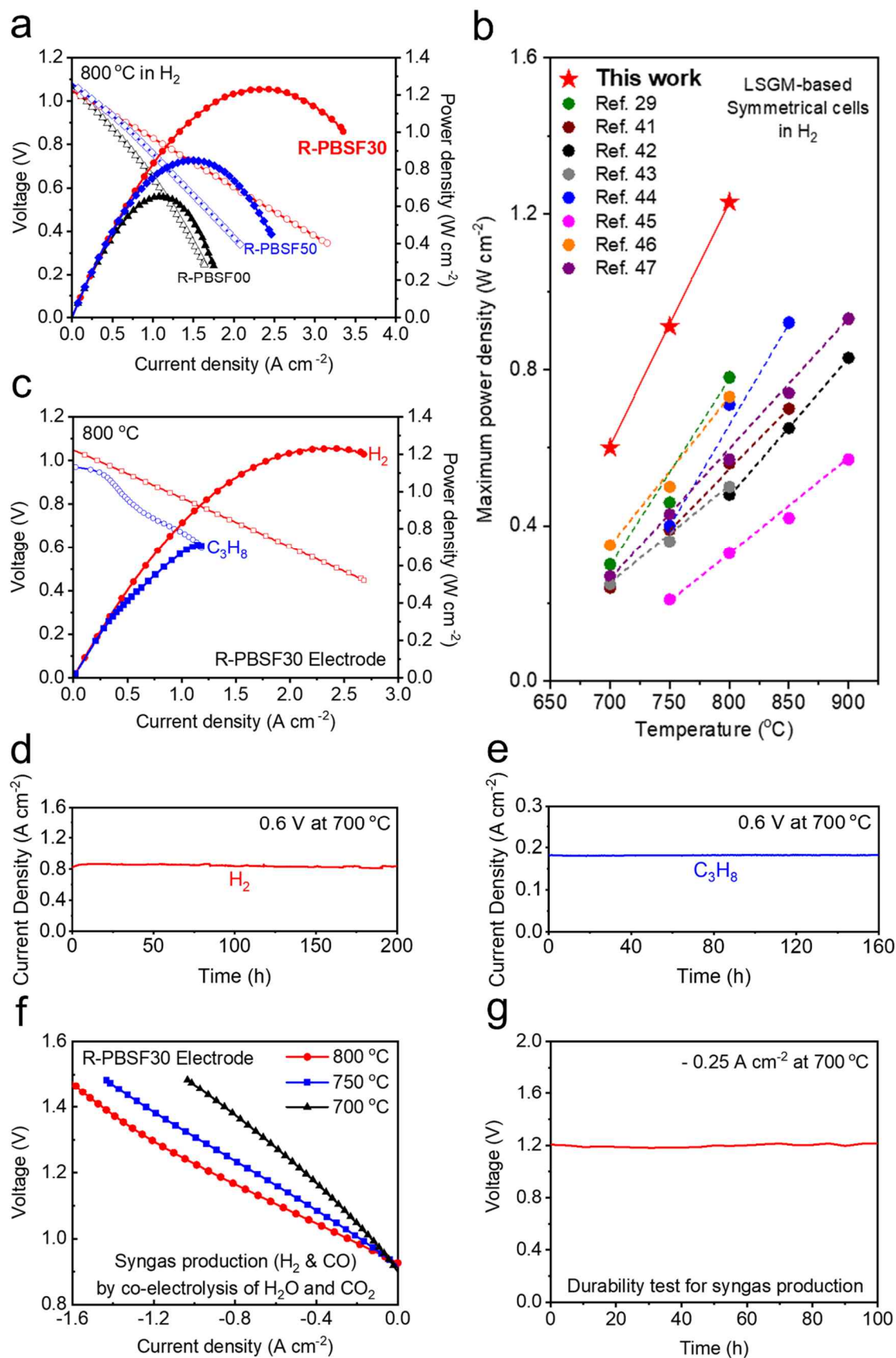


Figure 4. (a – b) Comparison of the maximum power density values at 800 °C in H₂ (a) in terms

of $\text{Pr}_{0.5}\text{Ba}_{0.5-x}\text{Sr}_x\text{FeO}_{3-\delta}$ compositions ($x = 0, 0.3, \text{ and } 0.5$) and (b) of the present work and other LSGM electrolyte-supported studies with symmetrical cell configuration at various temperature regimes. (c) I-V curves and the corresponding power densities of symmetrical cell with $(\text{Pr}_{0.5}\text{Ba}_{0.2}\text{Sr}_{0.3})_2\text{FeO}_{4+\delta}$ -Fe metal (R-PBSF30) fuel electrode at $800\text{ }^\circ\text{C}$ under H_2 and C_3H_8 humidified fuels (3% H_2O) fed on the fuel electrode and air fed on the air electrode. (d – e) Durability test of symmetrical cell with R-PBSF30 fuel electrode recorded with respect to time at a constant voltage of 0.6 V at $700\text{ }^\circ\text{C}$ under (d) H_2 and (e) C_3H_8 humidified fuels. (f) I-V curves for symmetrical cell with R-PBSF30 fuel electrode with humidified H_2 and CO_2 with H_2O co-fed to the fuel electrode side and air fed to the air electrode. (g) Durability test of symmetrical cell with R-PBSF30 fuel electrode recorded at a constant current of -0.25 A cm^{-2} at $700\text{ }^\circ\text{C}$ during co-electrolysis for 100 hours.

Table 1. Comparison of the electrochemical performance of LSGM electrolyte-supported symmetrical solid oxide fuel cells (S-SOFCs) reported in the literature and in the present study.

Reference	Cell configuration (Air electrode Electrolyte Fuel electrode)	Electrolyte thickness (μm)	Maximum Power Density at 800 °C (W cm^{-2})
Present study	A-PBSF30 LDC LSGM LDC R-PBSF30	~ 250	1.23
(28)	$\text{Pr}_{0.4}\text{Sr}_{0.6}\text{Co}_{0.2}\text{Fe}_{0.7}\text{Nb}_{0.1}\text{O}_{3-\delta}$ LSGM $\text{Pr}_{0.8}\text{Sr}_{1.2}(\text{Co,Fe})_{0.8}\text{Nb}_{0.2}\text{O}_{4+\delta}$ – CFA (Co-Fe alloy)	~ 300	0.78
(39)	$\text{Sr}_2\text{Ti}_{0.8}\text{Co}_{0.2}\text{FeO}_6$ LSGM $\text{Sr}_2\text{Ti}_{0.8}\text{Co}_{0.2}\text{FeO}_6$	~ 270	0.56
(40)	$\text{Sr}_2\text{Fe}_{1.5}\text{Mo}_{0.5}\text{O}_{6-\delta}$ LSGM $\text{Sr}_2\text{Fe}_{1.5}\text{Mo}_{0.5}\text{O}_{6-\delta}$	~ 265	0.48
(41)	$\text{Pr}_{0.6}\text{Sr}_{0.4}\text{Fe}_{0.7}\text{Ni}_{0.2}\text{Mo}_{0.1}\text{O}_{3-\delta}$ GDC LSGM GDC $\text{Pr}_{0.6}\text{Sr}_{0.4}\text{Fe}_{0.7}\text{Ni}_{0.2}\text{Mo}_{0.1}\text{O}_{3-\delta}$	~ 320	0.50
	$\text{Pr}_{0.6}\text{Sr}_{0.4}\text{Fe}_{0.8}\text{Ni}_{0.2}\text{O}_{3-\delta}$ GDC LSGM GDC $\text{Pr}_{0.6}\text{Sr}_{0.4}\text{Fe}_{0.8}\text{Ni}_{0.2}\text{O}_{3-\delta}$	~ 320	0.44
(42)	$\text{PrBa}(\text{Fe}_{0.8}\text{Sc}_{0.2})_2\text{O}_{5+\delta}$ LSGM $\text{PrBa}(\text{Fe}_{0.8}\text{Sc}_{0.2})_2\text{O}_{5+\delta}$	~ 275	0.71
(43)	$\text{SmBaMn}_2\text{O}_{5+\delta}$ LSGM $\text{SmBaMn}_2\text{O}_{5+\delta}$	~ 300	0.33
(44)	$\text{La}_{0.5}\text{Sr}_{0.5}\text{Fe}_{0.9}\text{Mo}_{0.1}\text{O}_{3-\delta}$ LSGM SDC $\text{La}_{0.5}\text{Sr}_{0.5}\text{Fe}_{0.9}\text{Mo}_{0.1}\text{O}_{3-\delta}$	~ 300	0.73
(45)	$\text{La}_{0.6}\text{Sr}_{0.4}\text{Co}_{0.2}\text{Fe}_{0.7}\text{Mo}_{0.1}\text{O}_{3-\delta}$ SDC LSGM SDC $\text{La}_{0.6}\text{Sr}_{0.4}\text{Co}_{0.2}\text{Fe}_{0.7}\text{Mo}_{0.1}\text{O}_{3-\delta}$	~ 270	0.74

A-PBSF30: $\text{Pr}_{0.5}\text{Ba}_{0.2}\text{Sr}_{0.3}\text{FeO}_{3-\delta}$

R-PBSF30: $(\text{Pr}_{0.5}\text{Ba}_{0.2}\text{Sr}_{0.3})_2\text{FeO}_{4+\delta}$ – Fe metal

LDC: $\text{La}_{0.4}\text{Ce}_{0.6}\text{O}_{2-\delta}$

GDC: $\text{Gd}_{0.4}\text{Ce}_{0.6}\text{O}_{2-\delta}$

SDC: $\text{Sm}_{0.4}\text{Ce}_{0.6}\text{O}_{2-\delta}$

LSGM: $\text{La}_{0.9}\text{Sr}_{0.1}\text{Ga}_{1-y}\text{Mg}_y\text{O}_{3-\delta}$ ($y = 0.15$ or 0.2)

Figures

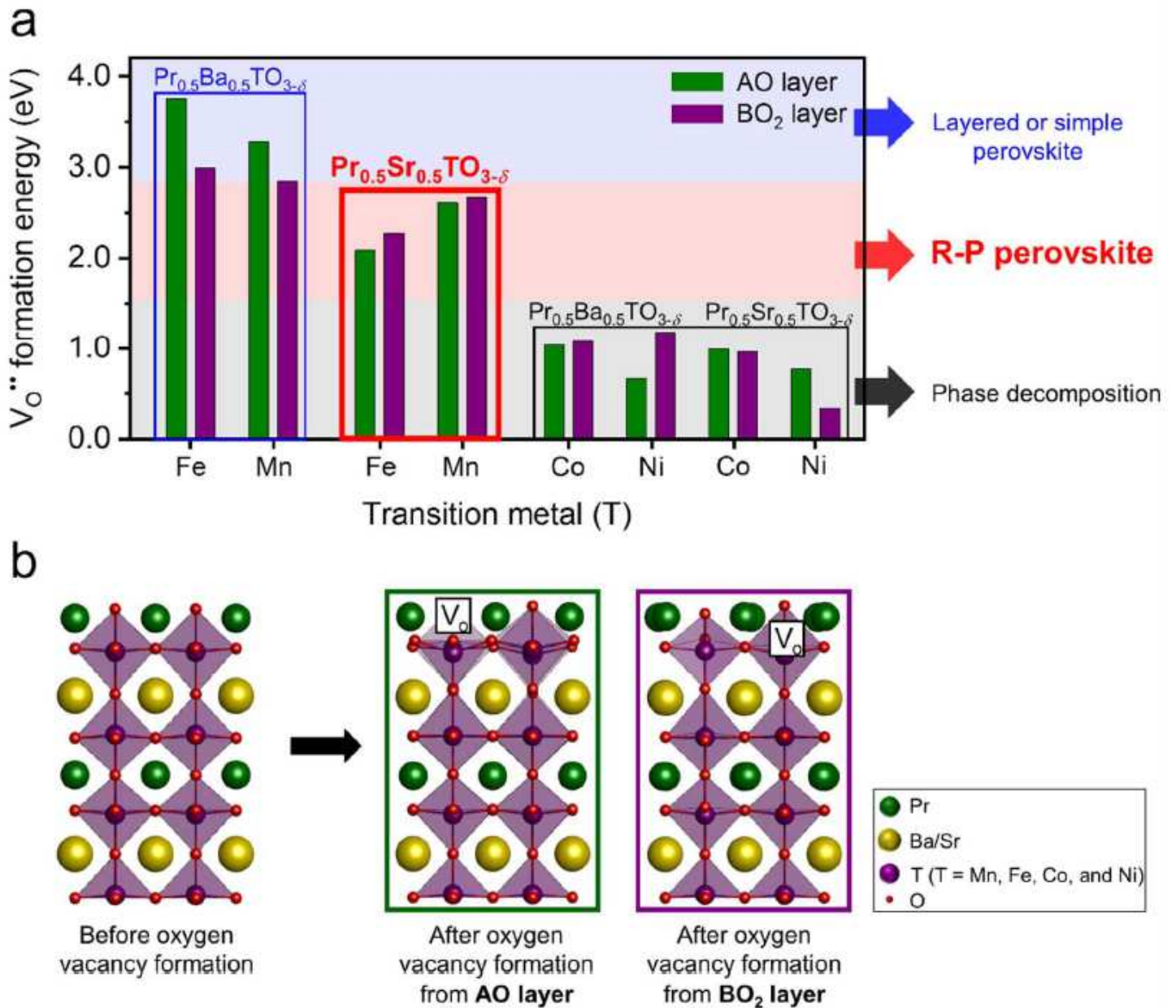


Figure 1

(a) Calculated oxygen vacancy formation energies of $Pr_{0.5}(Ba/Sr)_{0.5}TO_{3-d}$ (T = Mn, Fe, Co, and Ni) from AO (green bar) and BO_2 (purple bar) networks and the predicted phase change under reducing condition. (b) Schematic of the most stable structure configurations of $Pr_{0.5}(Ba/Sr)_{0.5}TO_{3-d}$ (T = Mn, Fe, Co, and Ni) slab models used for the calculations of oxygen vacancy formation energy values from AO and BO_2 networks.

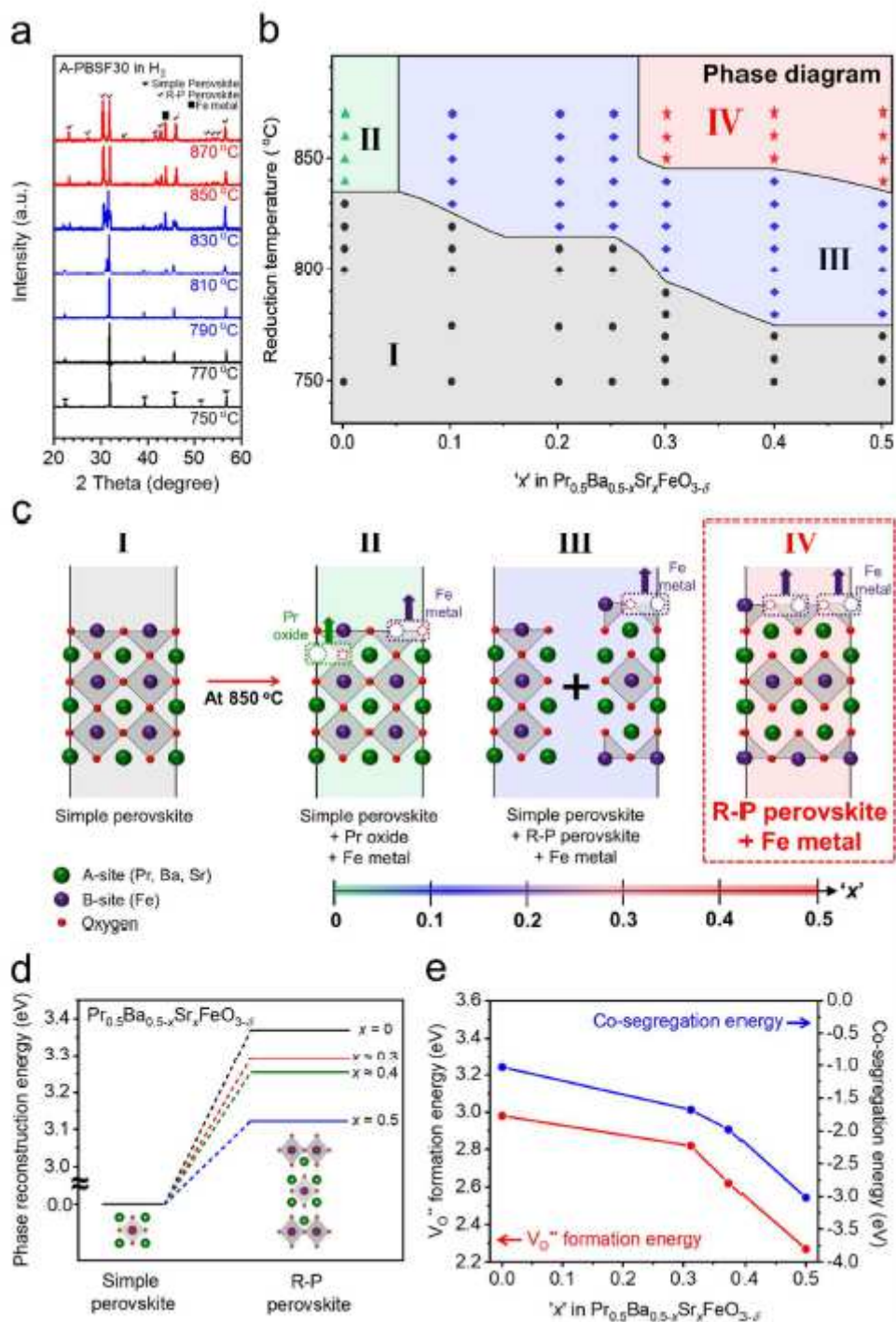


Figure 2

(a – c) Phase reconstruction tendency of Pr_{0.5}Ba_{0.5-x}Sr_xFeO_{3-d} material ($x = 0, 0.1, 0.2, 0.25, 0.3, 0.4$ and 0.5). (a) In-situ powder X-ray diffraction (XRD) patterns of Pr_{0.5}Ba_{0.2}Sr_{0.3}FeO_{3-d} (A-PBSF30) under H₂ environment. (b) Proposed phase diagram of Pr_{0.5}Ba_{0.5-x}Sr_xFeO_{3-d} material ($x = 0, 0.1, 0.2, 0.25, 0.3, 0.4$ and 0.5) in H₂ environment as functions of reduction temperature and Sr²⁺ concentration from in-situ X-ray diffraction (XRD) measurements. The phases for region I (gray), II (green), III (blue), and IV (red) are simple perovskite, simple perovskite + Pr oxide + Fe metal, simple perovskite + Ruddlesden-Popper (R-P) perovskite + Fe metal, and R-P perovskite + Fe metal, respectively. (c) Schematic illustration of the above

phase diagram. (d – e) Density functional theory (DFT) calculations. Calculated profiles of (d) the relative total energy required for the phase reconstruction from simple perovskite to R-P perovskite and (e) oxygen vacancy formation energies and cosegregation energies as a function of Sr²⁺ concentration in four models.

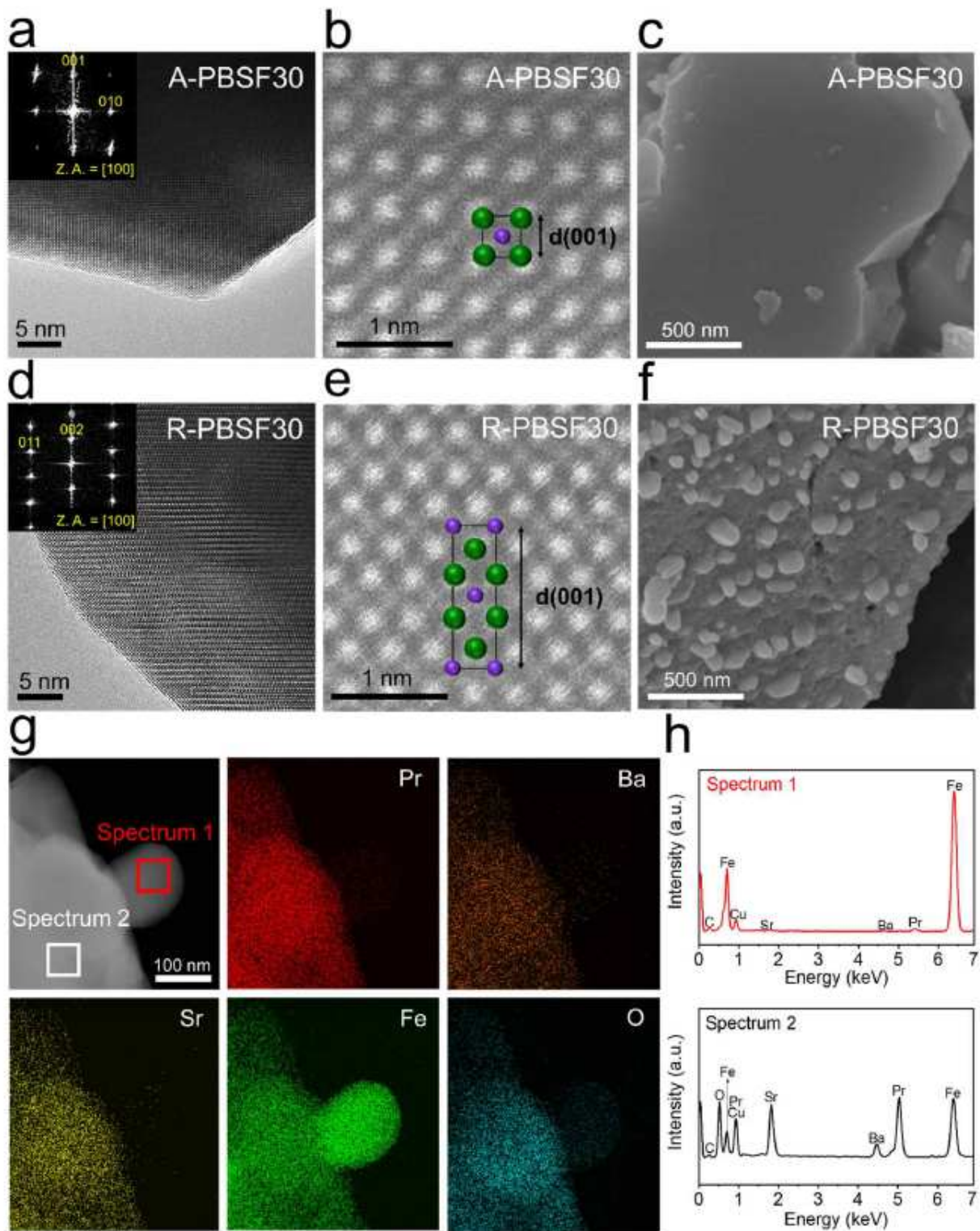


Figure 3

Electron microscopic analysis. (a – b, d – e) Transmission electron microscopy (TEM) analysis. (a) High-resolution (HR) TEM image and the corresponding fast-Fourier transformed (FFT) pattern of $\text{Pr}_{0.5}\text{Ba}_{0.2}\text{Sr}_{0.3}\text{FeO}_{3-d}$ (A-PBSF30) with zone axis (Z.A.) = [100] and (b) Highangle annular dark-field (HAADF) scanning TEM (STEM) image of A-PBSF30 with simple perovskite structure of [100] direction with d-spacing 001. (d) HR TEM image and the corresponding FFT pattern of $(\text{Pr}_{0.5}\text{Ba}_{0.2}\text{Sr}_{0.3})_2\text{FeO}_{4+d}$ – Fe metal (R-PBSF30) with Z.A. = [100] and (e) HAADF STEM image and the atomic arrangement of R-PBSF30 of [100] direction with d-spacing 001. (c,f) Scanning electron microscope (SEM) images. SEM images presenting the surface morphologies of (c) A-PBSF30 sintered at 1200 oC for 4 hours in air atmosphere and (f) R-PBSF30 reduced at 850 oC for 4 hours in humidified H₂ environment (3% H₂O). (g – h) TEM-energy dispersive spectroscopy (EDS) analysis. HAADF image of R-PBSF30 and elemental mapping of Pr, Ba, Sr, Fe and O, respectively. (h) EDS spectra of the exsolved Fe metal particle (Spectrum 1) and the parent material $(\text{Pr}_{0.5}\text{Ba}_{0.2}\text{Sr}_{0.3})_2\text{FeO}_{4+d}$ (Spectrum 2).

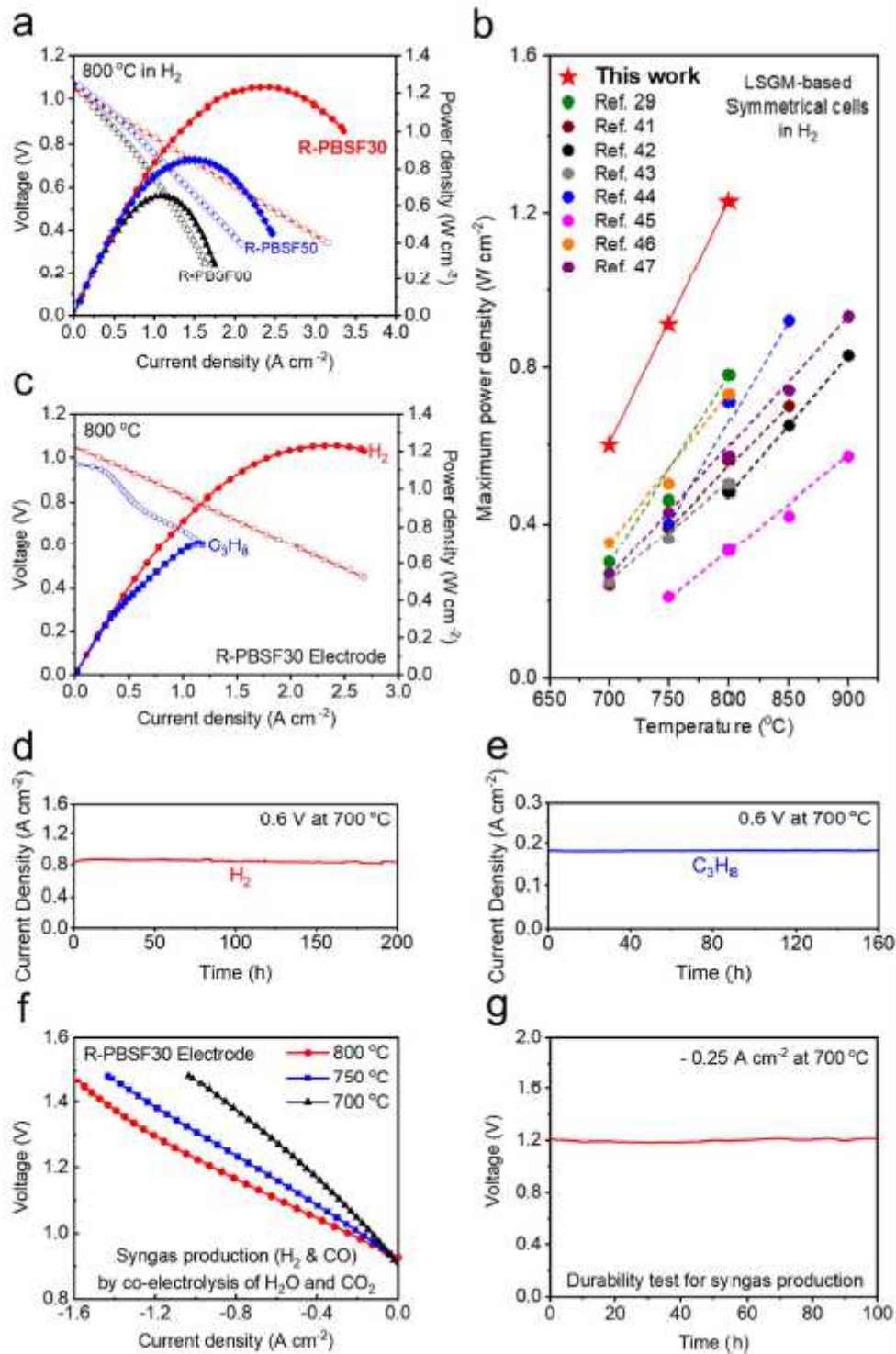


Figure 4

(a – b) Comparison of the maximum power density values at 800 °C in H₂ (a) in terms of Pr_{0.5}Ba_{0.5-x}Sr_xFeO_{3-d} compositions ($x = 0, 0.3, \text{ and } 0.5$) and (b) of the present work and other LSGM electrolyte-supported studies with symmetrical cell configuration at various temperature regimes. (c) I-V curves and the corresponding power densities of symmetrical cell with (Pr_{0.5}Ba_{0.2}Sr_{0.3})₂FeO_{4+d} – Fe metal (R-PBSF30) fuel electrode at 800 °C under H₂ and C₃H₈ humidified fuels (3% H₂O) fed on the fuel electrode

and air fed on the air electrode. (d – e) Durability test of symmetrical cell with R-PBSF30 fuel electrode recorded with respect to time at a constant voltage of 0.6 V at 700 oC under (d) H₂ and (e) C₃H₈ humidified fuels. (f) I-V curves for symmetrical cell with R-PBSF30 fuel electrode with humidified H₂ and CO₂ with H₂O co-fed to the fuel electrode side and air fed to the air electrode. (g) Durability test of symmetrical cell with R-PBSF30 fuel electrode recorded at a constant current of – 0.25 A cm⁻² at 700 oC during co-electrolysis for 100 hours.

Supplementary Files

This is a list of supplementary files associated with this preprint. Click to download.

- [SupplementaryinformationNatureCommunications.pdf](#)